Cell Reports
Physical Science

Article

Quantitative synthesis of dynamic combinatorial macrocycles accelerated by preorganization of AIEgens for live visualization of drug release

Graphical abstract

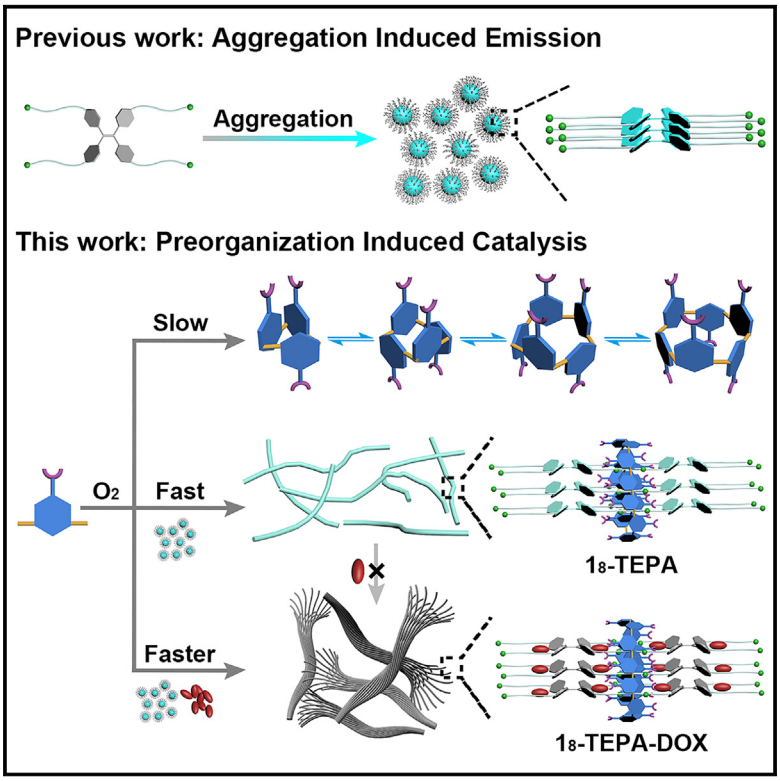

Highlights

- AIE-related preorganization catalyzes chemical reactions
- AIE's steric effects enhance selective production of the reaction
- The AIE-driven reaction creates nanosystems for visualizing drug release

Authors

Jinghui Yang, Xin Wang, Xiaoxia Wu, Yonglei Lyu, Anastassios C. Papageorgiou, Jianwei Li

Correspondence

jianwei.li@utu.fi

In brief

Jinghui et al. demonstrate that AIE preorganization catalyzes chemical reactions, with steric effects enhancing selectivity. The interplay of covalent and noncovalent interactions in the AIE-driven reaction shapes structure and optical properties, enabling a multicomponent nanosystem for real-time drug release visualization.

Yang et al., 2025, Cell Reports Physical Science 6, 102355
January 15, 2025
https://doi.org/10.1016/j.xcrp.2024.102355

CellPress

Cell Reports
Physical Science

CellPress
OPEN ACCESS

Article

Quantitative synthesis of dynamic combinatorial macrocycles accelerated by preorganization of AIEgens for live visualization of drug release

Jinghui Yang,[1,2] Xin Wang,[1,2] Xiaoxia Wu,[1] Yonglei Lyu,[1,2] Anastassios C. Papageorgiou,[3] and Jianwei Li[1,4,5,6,7,*]
[1]MediCity Research Laboratory, University of Turku, 20520 Turku, Finland
[2]Department of Chemistry, University of Turku, 20500 Turku, Finland
[3]Turku Bioscience Centre, University of Turku, Åbo Akademi University, 20520 Turku, Finland
[4]X (formerly Twitter): @uniturku
[5]X (formerly Twitter): @medicityl
[6]X (formerly Twitter): @jianwei_chem
[7]Lead contact
*Correspondence: jianwei.li@utu.fi
https://doi.org/10.1016/j.xcrp.2024.102355

SUMMARY

In the aggregated state, restricted molecular movement leads to decreased entropy, a phenomenon closely associated with the release of luminescence known as aggregation-induced emission (AIE). This unique optical property is used in optoelectronic devices, biochemical sensors, and bioimaging. Complementing AIE's optical characteristics, we report that AIE-related preorganization can catalyze chemical reactions, yielding highly selective products. These products can affect aggregation states, modulating fluorescence. Incorporating an anticancer drug into this system intensified entropy reduction, accelerated reactions, and altered nanostructure. The drug's electron-donating properties quench fluorescence via energy transfer with the AIE molecule. These components engage in reversible reactions and noncovalent interactions, creating responsive nanosystems for real-time drug release visualization in drug-resistant cancer cells. This synergy between AIE and *in situ* dynamic covalent reactions offers a promising strategy for synthesizing specific molecules and exploring adaptive nanosystems with advanced optical properties for biomedical applications.

INTRODUCTION

Dynamic combinatorial chemistry (DCC) has proven to be a powerful methodology for synthesizing complex molecular architectures, offering a versatile approach to creating adaptive systems that respond to environmental stimuli.[1–5] In DCC, a dynamic library of interconverting species is generated, where the most stable or "fittest" members, those that best interact with a given template, are selectively amplified through reversible reactions.[6,7] This process enables the selective synthesis of specific molecular entities, such as macrocycles, which hold significant potential for various applications, including drug delivery.[8–11]

A key challenge in DCC, however, is achieving both high efficiency and selectivity in the synthesis of desired species.[12–14] Here, we demonstrate that the preorganization of template molecules provides a solution to this challenge. By preorganizing the template molecules, the dynamic system can be directed toward the accelerated formation of specific target structures.[15] This preorganization effectively lowers the energy barriers associated with macrocyclization, thereby enhancing both the rate and selectivity of the process.[16–18]

In recent years, aggregation-induced emission luminogens (AIEgens) have gained significant attention due to their unique property of becoming highly emissive upon aggregation, an advantage in complex and dynamic environments.[19–25] Integrating AIEgens into DCC systems introduces an additional layer of control and functionality.[26–28] When AIEgens are employed as template molecules within preorganized dynamic systems, their inherent propensity to aggregate can be exploited to promote the selective and rapid synthesis of specific macrocycles.[29–32] This preorganization of AIEgen templates not only accelerates the formation of the desired structures but also endows the resulting macrocycles with intrinsic fluorescence, making them ideal for real-time monitoring.[33]

In our study, we utilized the classic thiol oxidation reaction in water to generate a variety of dynamic combinatorial macrocyclic disulfides. The final distribution of these species was influenced by their relative energy levels.[34] The introduction of an AIE-active molecule, specifically a tetraphenylethene derivative (**TPEA**), significantly accelerated the oxidation rate. Remarkably, a specific disulfide product, which was scarcely produced in the absence of **TPEA**, became the predominant species in the presence of this AIEgen. This outcome was attributed to the thermodynamic stabilization provided by noncovalent interactions between functional units of adjacent **TPEA** derivatives.[35,36] Additionally, the **TPEA**-induced nanostructure transitioned from

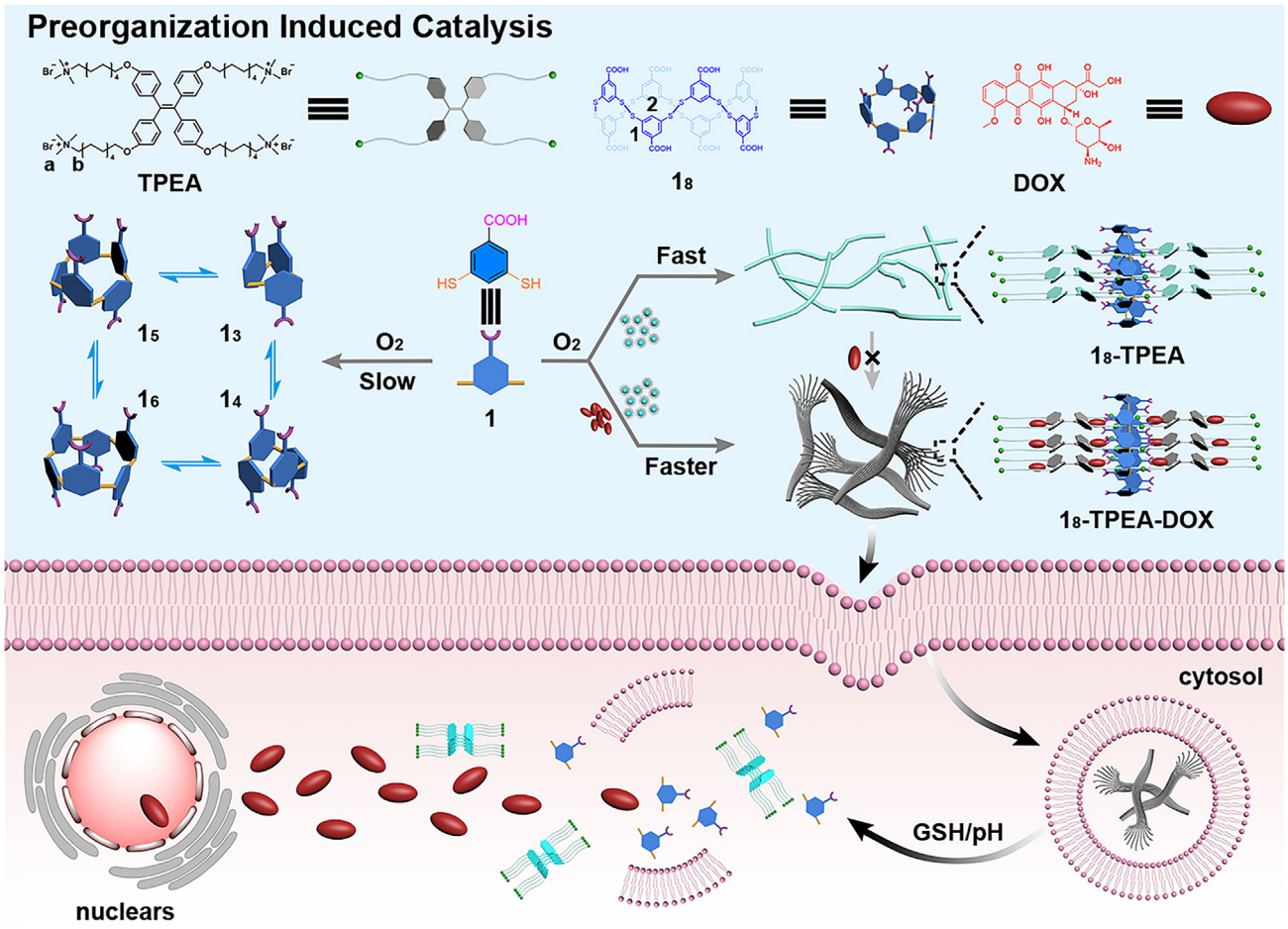

Scheme 1. Illustration of preorganizing nanosystems

This study on catalysis induced by preorganizing of templates in dynamic systems. Guided by an AIE template molecule, the thiol oxidation of a disulfide-based Dynamic Combinatorial Libraries (DCLs) was accelerated, selectively and quantitatively amplifying octameric disulfide macrocycle ($\mathbf{1_8}$). Introducing the anticancer drug DOX into the reactive system resulted in its encapsulation within the AIE aggregates, further decreasing entropy and accelerating thiol oxidation. Additionally, the morphology and fluorescence of the nanostructures adapted and responded to changes in the solution's pH and redox levels. This adaptability enabled *in situ* bioimaging for drug delivery against DOX-resistant cancer *in vitro*.

micelles to nanofibers, with a corresponding decrease in fluorescence intensity. However, when the same systems were conducted in acetonitrile, the **TPEA** templates were fully dissolved, and the fully oxidized library consisted of a mixture of multiple species. These findings suggest that the preorganization of **TPEA** facilitated thiol oxidation, while the adjacent functional groups in the aggregated state aided in the selective synthesis of the specific disulfide.

Further, by introducing the anticancer drug doxorubicin (DOX) into the system, we observed that its incorporation into the multicomponent self-assembly reduced the system's entropy and further accelerated the chemical reaction.[37] This process resulted in a nanosystem with dual responsiveness, capable of visualizing the drug delivery process.[38–40] These results highlight the synergy between AIE and *in situ* dynamic chemical reactions, suggesting a promising strategy for the efficient synthesis of specific molecules and the exploration of adaptive nanosystems with advanced optical properties.[41]

RESULTS AND DISCUSSION

Synthesis and characterization of the 1_8-TPEA nanofibers

To achieve AIE in water, the **TPEA** was functionalized with positively charged quaternary ammonium salt groups linked by alkyl chains to increase its water solubility while keeping its hydrophobicity (see Scheme 1).[30,36] Indeed, the **TPEA** molecule self-assembled into micelles with a diameter around 20 nm in a PBS buffer (pH 7.4) (Figure 1A), when its concentration was over the critical aggregation concentration (CAC) 2.1×10^{-6} M determined by fluorescence spectroscopy (Figure S1). Its AIE property was confirmed by measuring fluorescence in a mixed solution of water and acetonitrile (Figure S2). The **TPEA** exhibited non-fluorescence or weak fluorescence when dissolved in a solution with the higher percentage of acetonitrile than 40%, owing to its high solubility in this solvent. However, fluorescence emerged with an increasing water fraction in the medium

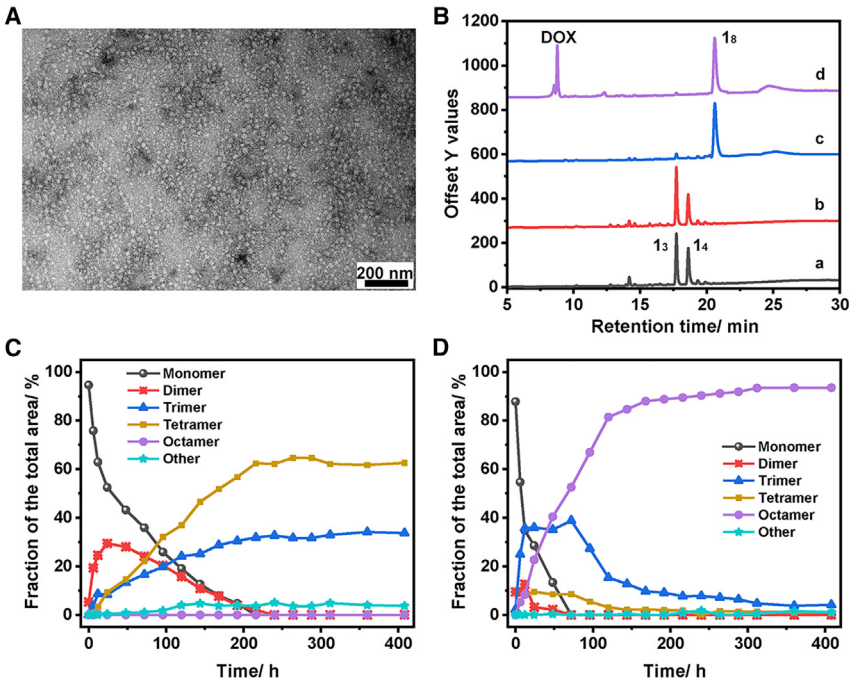

Figure 1. Characterization of 1_8-TPEA nanofiber and kinetic study

(A) TEM analysis of **TPEA** micelles. Scale bar: 200 nm.

(B) HPLC-MS analysis of fully oxidized DCLs made from (a) only building block **1** (1.0 mM), (b) building block **1** (1.0 mM) and **TPEA** (0.125 mM), (c) building block **1** (1.0 mM) and **TPEA** (0.25 mM), and (d) building block **1** (1.0 mM), **TPEA** (0.25 mM), and DOX (0.50 mM) in PBS buffers (50 mM, pH 7.4).

(C and D) Kinetic study for DCLs made from (C) only the building block **1** (1.0 mM) and (D) the building block **1** (1.0 mM) and **TPEA** (0.25 mM) in PBS buffers (50 mM, pH 7.4).

due to the lowering of the solubility of **TPEA**. Encouraged by such an excellent AIE property of **TPEA**, we proceed to verify whether the preorganization of AIE templates could serve as a catalyst for chemical reactions. A dithiol building block **1** was chosen as the starting molecule for the reaction. It (1.0 mM) could be oxidized to generate disulfide macrocyclic molecules in a PBS buffer (pH 7.4) at room temperature by the oxygen in the air. The kinetics of the oxidation reaction was monitored by high-performance liquid chromatography-mass spectrometry (HPLC-MS), suggesting that the full oxidation was reached after 9 days, and the main products were trimeric macrocycle ($\mathbf{1_3}$) and tetrameric macrocycle ($\mathbf{1_4}$) (see Figures 1B and 1C). In parallel, a control experiment was designed by running the same reaction but with the participation of **TPEA** molecules (0.25 mM) in the same solution. Remarkably, the oxidation process was shortened to 3 days (see Figures 1B and 1D), which revealed that the reaction was accelerated 3-fold. To show the detailed oxidation kinetics of thiols, we monitored their concentration changes over time using Ellman's method (see Figures S6 and S7). By comparing the oxidation profiles of thiols in the absence and presence of **TPEA**, we observed a significant acceleration in the oxidation rate with **TPEA**. Specifically, the overall oxidation rate in the presence of **TPEA** was three times higher than without it, confirming the results determined by HPLC peak areas (see Figures S8 and S9). To examine the relationship between the fluorescence intensity of **TPEA** and the oxidation process, we also studied the kinetics of fluorescence changes of a diluted library consisting of **1** (1.0 mM) and **TPEA** (0.25 mM) in PBS buffer (50 mM, pH 7.4). After the building block and **TPEA** are mixed, the fluorescence of **TPEA** undergoes a blue shift. With the oxidation of building block **1**, the fluorescence gradually decreased and finally stabilized, showing a similar trend to the thiol concentration decrease during the oxidation (see Figure S10). Compared with the florescence intensity of **TPEA** alone, that of the **TPEA** in the end of the reaction was decreased by 41.1% (Figure 2A). We reasoned that the preorganizing of **TEPA** with dynamic systems should speed up chemical reactions.

Interestingly, the presence of **TPEA** in the reaction also resulted in the quantitative production of a specific disulfide product octamer ($\mathbf{1_8}$) (see Figure S4). At the same time, the morphology of **TPEA** transformed into nanofibers with a width of 3.7 nm from the micelles (see Figure 2). Since this width resembled the width of the **TPEA** molecules (see Figure S3), they probably stacked in line to form the nanofibers. The further comparation of fluorescence spectra of **TPEA** after the oxidation in water showed a blue shift, suggesting an H-aggregation (see Figure 2A).[42,43]

We proceeded to understand the highly selective production. First, the zeta potential of the micelles self-assembled by only **TPEA** was determined as +8.4 mV, while that of the nanofiber was +6.6 mV (see Figure S5). This more negatively shifted value should result from the complexation of the negatively charged $\mathbf{1_8}$ with the positively charged surface of **TPEA** aggregation. Subsequently, we tried to investigate the molecular organization of the nanofiber by analyzing the fully oxidized reaction mixture in D_2O (pD 7.4) using ^{1}H-nuclear magnetic resonance (^{1}H-NMR) technologies. Unfortunately, no signal was observed due to the severally decreased tumbling rate in solution arising from the complete aggregation for the formation of the nanostructure. Therefore, instead of studying the fully oxidized sample, we focused on the analysis of the sample at the initial stage of oxidation to get insights into the interaction between **building block 1** and **TPEA** using NMR. In the presence of **TPEA**, the H2 proton of **building block 1** shifted upfield, and its spin-spin relaxation (T2 relaxation) time decreased markedly from 3,049 to 608.4 ms (see Figure S11). These results suggest that **building block 1** entered the hydrophobic region of the pre-assembled AIEgens, resulting in restricted molecular motion and an enhancement in electrostatic interactions between the components, which should help the synthesis of $\mathbf{1_8}$. Considering that the electrostatic complementarity was the main driving force for the binding between the **TPEA** and $\mathbf{1_8}$, we used a cationic surfactant octadecyl

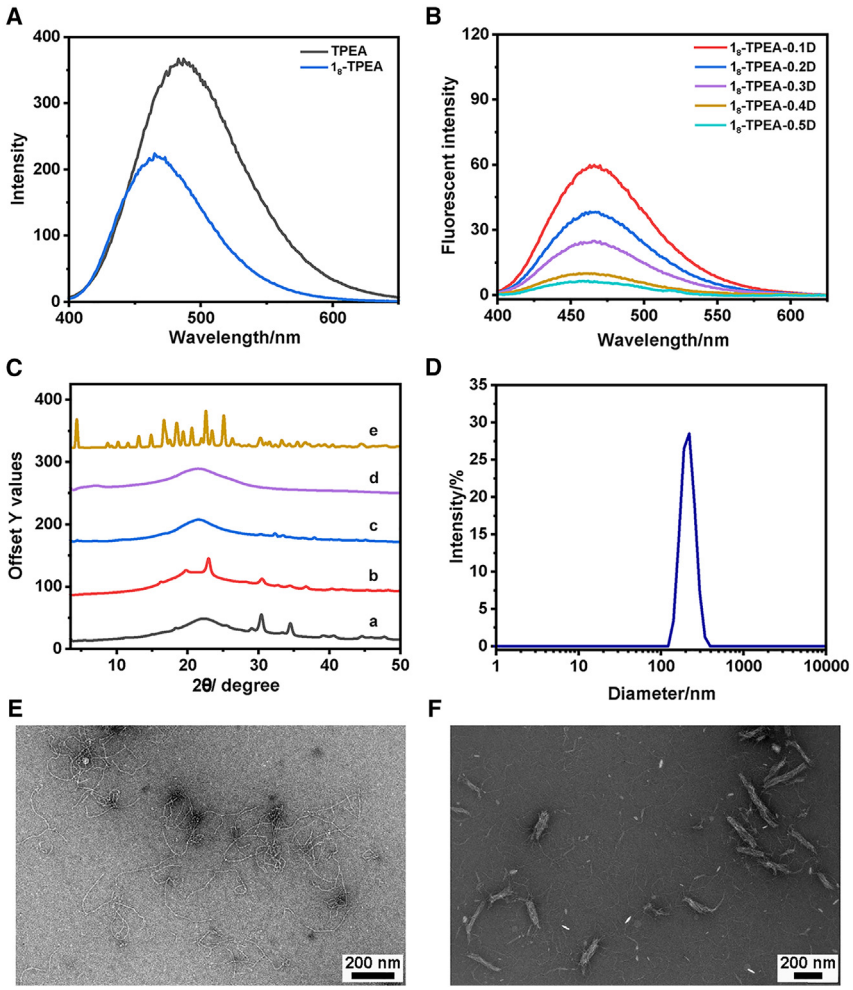

Figure 2. Characterization of 1_8-TPEA-DOX nanofiber bundles

(A) Fluorescence spectra of a **TPEA** (10 μM) solution and a diluted library **1_8-TPEA** consisting of **1_8** (5 μM) and **TPEA** (10 μM) in PBS buffer (50 mM, pH 7.4). **TPEA** λ_{ex} = 330 nm.

(B) Fluorescence analysis of diluted libraries **1_8-TPEA**-DOX containing **1_8** (5 μM), **TPEA** (10 μM), and DOX with various concentrations ranging from 0.1 to 0.5 equiv of building block **1** in PBS buffer (50 mM, pH 7.4).

(C) PXRD analysis of (a) **1_3** + **1_4**, (b) **TPEA**, (c) **1_8-TPEA**, (d) optimized ratio of **1_8-TPEA**-DOX, and (e) DOX.

(D) Size distribution in **1_8-TPEA**-DOX library analyzed by DLS at room temperature.

(E and F) TEM analysis of (E) **1_8-TPEA** and (F) **1_8-TPEA**-DOX libraries. Scale bar: 200 nm.

trimethyl ammonium bromide (OTAB) equipped with the same quaternary ammonium salt group to elucidate the noncovalent interactions (for structures, see Figure S12). Upon addition of the **1_8** into a solution of the template OTAB in D_2O (2 mM, pD 7.4), the signals of the methyl protons of trimethyl ammonium units and the methylene protons (H_a and H_b) of the template showed remarkable upfield shifts, while the signal of the aromatic protons H_1 and H_2 of **1_8** moved downfield. These complementary changes of chemical shifts should be the result of the electrostatic interaction between the deprotonated carboxylic acid groups on hosts and the positively charged ammonium salts as guests.[35]

To further understand the spatial conformation of the inclusion complex, we also conducted two-dimensional nuclear Overhauser effect (2D NOESY) experiments. The NOE correlation signals were observed between protons on the **1_8** and the H_a and H_b on the template, confirming the above threading binding mode. The complex stoichiometry between **1_8** and the **TPEA** was 1:2, determined by the Job's plot method on a fluorescence spectrophotometer (see Figure S13). The binding constant was further determined using the fluorescence titration method under various experimental conditions (see Figure S14). A binding constant of 6.2 × 10^5 M^{-1} was obtained in PBS buffer (50 mM, pH 7.4) at room temperature. A slight decrease in the binding constant was noted at lower pH levels, while temperature variations had a minimal effect, indicating excellent binding stability across different temperatures. The minor reduction in binding strength at lower pH likely resulted from the protonation of the carboxyl group, which weakened the electrostatic interactions between **1_8** and **TPEA**. These results revealed that one **1_8** molecule was strongly associated with two quaternary ammonium salt groups from two adjacent **TPEA** molecules. To verify this hypothesis, we prepared a library with the same concentrations as before, using building block **1** (1.0 mM) and **TPEA** (0.25 mM), but this time in a solution containing 70% acetonitrile by volume in water. The addition of acetonitrile, which dissolved the **TPEA** aggregates as indicated by the quenching of fluorescence, likely increased the spacing between the quaternary ammonium salt groups. As a result, the trimer (**1_3**) emerged as the predominant species, while the **1_8** nearly vanished in this specific library setup (see Figure S15). Altogether, the quantitative yield of **1_8** should be driven by the strong surface binding of the pre-assembled **TPEA**, and the molecular organization of the nanofiber consisting of **TPEA** and **1_8** is shown in Figure S16.

Synthesis and characterization of the 1_8-TPEA-DOX nanofiber bundles

Furthermore, apart from the investigation of only **TPEA** molecules, we also introduced another anticancer drug, DOX, into the system. It is well known that DOX can be encapsulated into the hydrophobic domain of supramolecular nanostructures. A previous work[44] has reported that the freedom degree of drug molecules would be reduced after the encapsulation process occurred and that the entropy of the whole chemical system should decrease more. Based on this conclusion, we expected

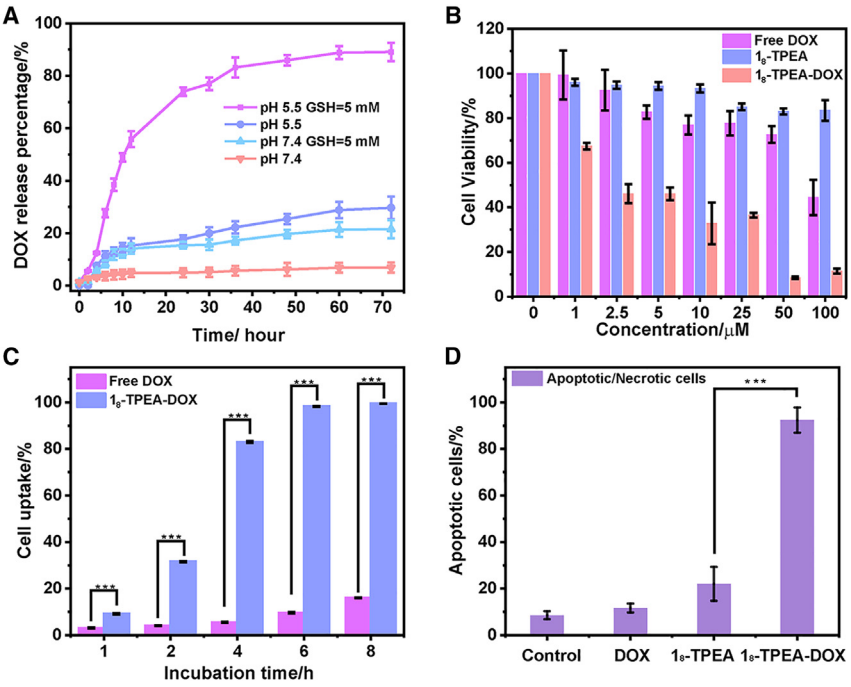

Figure 3. 1_8-TPEA-DOX nanofiber bundles show enhanced anti-proliferation efficiency via rapid, effective drug release, cellular uptake, and drug efflux inhibition

(A) Time course of DOX released from nanobundles of the **1_8-TPEA**-DOX at pH 5.5, 7.4 and pH 5.5, 7.4 with 5 mM GSH at 37°C.

(B) The anti-proliferative activity of free DOX, **1_8-TPEA** nanofibers, and **1_8-TPEA**-DOX nanofiber bundles on drug-resistant NCI/RES-ADR cells were measured by MTT assay.

(C) The cellular uptake in drug-resistant NCI/RES-ADR cells was quantified using flow cytometry after treatment with free DOX (C_{DOX} = 10.0 μM) and **1_8-TPEA**-DOX (C_{DOX} = 10.0 μM) at 1, 2, 4, 6, and 8 h.

(D) Quantitative analysis of Annexin V-positive cells after treatment with nontreatment control, free DOX, **1_8-TPEA**, and **1_8-TPEA**-DOX after 4 h. All the measurements were performed at least in triplicate; error bars represent SDs about the mean. *$p < 0.05$, **$p < 0.01$, and ***$p < 0.001$.

that such an entropy decrease should be compensated by releasing more energy to obey the second law of thermodynamics, and the energy release may be presented by driving the thiol oxidation more quickly. Thus, we tested the DCLs prepared from the same concentrations of building block **1** (1.0 mM) and **TPEA** (0.25 mM) with varying concentrations of DOX and observed fluorescence quenching (Figure 2B). Additionally, the octamer **1_8** remained the dominant species, but its production was 4.8 times faster in the presence of DOX (0.4 mM) compared to the library made with the same concentrations of building block **1** and **TPEA** (see Figure S17). These results further validate our concept of utilizing pre-assembly to catalyze selective synthesis in dynamic systems.

Notably, the fluorescence was quenched almost completely when the DOX concentration reached 0.50 mM (Figure 2B). This quenching phenomenon was attributed to energy transfer relay (ETR) by the overlap between the emission of **TPEA** and the absorption of DOX (Figure S18).[39] The maximum drug loading capacity of **1_8-TPEA**-DOX achieved was 31.8%, with a corresponding encapsulation efficiency of 93.5%. At this optimized ratio (**1_8**:**TPEA**:DOX = 0.125:0.25:0.5 mM), the morphology of the complex chemical system had a new adaption to fiber bundles with an approximate dimension of 50 × 220 nm determined by transmission electron microscopy (TEM), which was consistent with the Z-average size of 260 nm measured via dynamic light scattering (DLS) analysis (see Figures 2D and 2F). Additionally, the disappearance of the DOX signal in power X-ray diffraction (PXRD) analysis indicated that DOX was fully encapsulated in a non-crystalline form within the newly formed nanosystem (see Figure 2C). Given the amphiphilicity of DOX and the observed fluorescence quenching, it is suggested that DOX molecules are likely embedded in the hydrophobic region of **1_8-TPEA**-DOX, near the **TPEA** core.[45] Interestingly, adding DOX into the oxidized library containing **1_8-TPEA** nanofibers failed to disperse and encapsulate effectively, suggesting that the thiol-disulfide exchange had significant kinetic control over the drug encapsulation and nanomorphological evolution process.

Considering that the optical property was highly dependent on the composition of the multicomponent nanosystem and the nanosystem was organized by noncovalent interactions and reversible chemical reactions, we reasoned that the system should be dynamic and responsive. Thus, together with the high drug loading content of the **1_8-TPEA**-DOX composite, this nanosystem held great potential as an excellent drug delivery system for cancer therapy while imaging the drug release in real time to better understand its pharmacokinetics and pharmacodynamics.

Redox- and pH-induced release of DOX and TPEA from the nanofiber bundles

Keeping these results in mind, we moved forward to first evaluate the responsiveness of the **1_8-TPEA**-DOX nanosystem. In the context of drug delivery, it is crucial to control the drug release profile at tumor sites. Tumor cells typically exhibit a more acidic environment than normal cells due to the accumulation of lactic acid and CO_2 in a hypoxic microenvironment.[46] Additionally, the concentration of glutathione (GSH) inside cancer cells, exceeding 5 mM, is significantly higher than that in the extracellular matrices at tumor sites.[47,48] Consequently, we applied these dual stimuli to simulate the biological and endo-lysosomal environments and monitor the release profile of DOX and **TPEA** *in vitro* (Figure 3A). The cumulative release of DOX was <7% at pH 7.4, indicating that the **1_8-TPEA**-DOX nanofiber bundles remained stable under physiological pH conditions. However, at the endo-lysosomal pH of 5.5 in the presence of GSH, the release of DOX from the **1_8-TPEA**-DOX nanofiber bundles was significantly accelerated. Within 24 h, nearly 80% of the

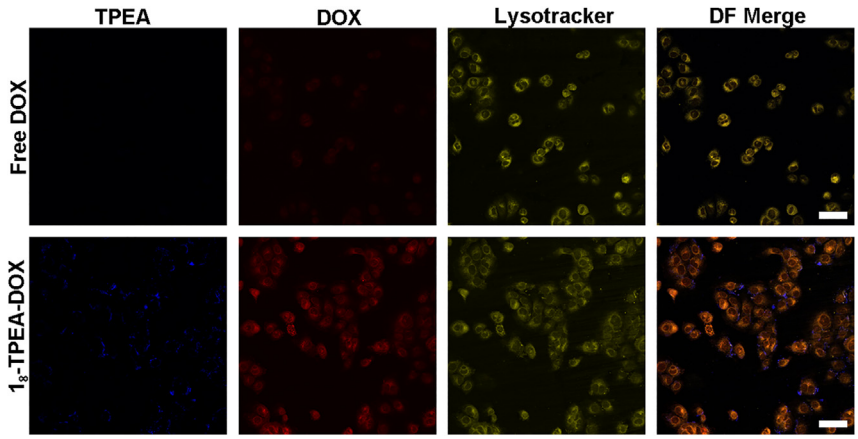

Figure 4. The cellular uptake was imaged using a confocal microscope

Images of NCI/ADR-RES cells incubated with free DOX and **1_8-TPEA**-DOX nanofiber bundles at a DOX concentration of 10 μM for 4 h. Blue, red, and yellow fluorescence indicate **TPEA**, DOX, and the LysoTracker, respectively. Scale bar, 50 μm.

total DOX in the nanofiber bundles was released, while the cumulative leakage was <18% over the same period at pH 5.5 without GSH. Under physiological conditions, the deprotonation of carboxylic groups of **1_8** enhanced the electrostatic interaction with the positive charge of **TPEA**, thereby maintaining the stability of the nanostructure. However, as the pH became acidic (pH 5.5), the carboxylate anions of **1_8** were protonated, as indicated by a decrease in solubility compared to that observed at pH 7.4 (see Figure S19). The protonation would weaken the electrostatic interaction and render the entire nanofiber bundle fragile, resulting in the release of DOX. Furthermore, the amine-bearing DOX loaded in the system became more positively charged at low pH, increasing the solubility of DOX (see Figure S19), further promoting drug release.[49–51]

Following the establishment of the favorable drug release profile of **1_8-TPEA**-DOX nanofiber bundles, we conducted a comprehensive evaluation of their anti-proliferative efficiency in NCI/RES-ADR DOX-resistant human breast ovarian cancer cells. As depicted in Figure 3B, the IC_{50} value of free DOX for NCI/RES-ADR cells was approximately 100 μM. The pronounced resistance to DOX observed was attributed to the overexpression of P-glycoprotein (P-gp) by NCI/RES-ADR cells. P-gp functions by pumping DOX molecules out of cancer cells. However, DOX resistance could be overcome by nanofiber bundles that inhibited P-gp efflux and depleted adenosine triphosphate (ATP). Notably, the IC_{50} value of **1_8-TPEA**-DOX nanofiber bundles for NCI/RES-ADR cells was 3.2 μM, remarkably lower than that (100 μM) of free DOX, signifying a 30-fold increase in toxicity. This outcome unequivocally demonstrated the substantial superiority of **1_8-TPEA**-DOX nanofiber bundles over free DOX in enhancing cell anti-proliferation in drug-resistant cell lines.[8]

Enhanced cellular uptake of the nanofiber bundles

To gain insights into the mechanism underlying the enhanced proliferation inhibition by **1_8-TPEA**-DOX nanofiber bundles, we examined their cellular uptake in NCI/RES-ADR cells using flow cytometry analysis. The drug uptake efficiencies in NCI/RES-ADR cells were approximately 3% and 5% after incubation with free DOX at 10 μM for 1 and 4 h, respectively. In contrast, drug uptake reached nearly 90% after a 4 h incubation with **1_8-TPEA**-DOX nanofiber bundles (10 μM DOX) (Figure 3C). This observation strongly suggests that DOX-loaded nanofiber bundles significantly enhance the time-dependent cellular internalization and accumulation of DOX. Collectively, these results clearly demonstrated that **1_8-TPEA**-DOX nanofiber bundles were much more effective than free DOX in enhancing anti-proliferation efficiency in DOX-resistant NCI/RES-ADR cells, ultimately leading to apoptosis-induced anticancer activity (Figure 3D).

We validated the augmented cellular uptake of **1_8-TPEA**-DOX nanofiber bundles in NCI/RES-ADR cells using confocal laser scanning microscopy (CLSM). When free DOX was employed, the red fluorescence was barely detectable in cancer cells and did not induce cytotoxicity. Following 4 h incubation of NCI/RES-ADR cells with **1_8-TPEA**-DOX nanofiber bundles, DOX fluorescence was observed in both the cytoplasm and nucleus. Simultaneously, **TPEA** fluorescence appeared in the cytoplasm, with no **TPEA** signal observed in the nucleus. This observation indicated that the carrier solely served its delivery function and did not influence the anticancer effect of DOX. Notably, each cell contained a substantial cytoplasm displaying a notably strong fluorescence signal from both **TPEA** and DOX. We hypothesized that this cytoplasm region corresponded to lysosomes, where the detachment of DOX from the **1_8-TPEA**-DOX nanofiber bundles led to a fluorogenic response. To test this, we stained lysosomes with LysoTracker Deep Red (Figure 4, Dual Field [DF] merge) and found that the strong **TPEA** and DOX signals did indeed colocalize with lysosomes. These results further confirmed that the **1_8-TPEA**-DOX nanofiber bundles were responsive to low pH and GSH in cancer cells, and **TPEA** and DOX were released in lysosomes.

Real-time visualization release of DOX and TPEA from the nanofiber bundles *in vitro*

Real-time visualization of drug release will enable us to understand this process better and will enlighten future designs of sophisticated nanocarriers. Our **1_8-TPEA**-DOX bundle is well suited to this purpose. The pH and GSH induce a dual-color fluorogenic response from both **TPEA** and DOX once the DOX is released. To achieve real-time visualization of the drug release at the subcellular level and observe subtle changes at each time point during this process, we employed a real-time CLSM system equipped with a continuous shooting apparatus. This non-invasive method eliminates the need for cell disruption or organelle isolation. NCI/RES-ADR cells were incubated with **1_8-TPEA**-DOX and monitored using real-time CLSM, capturing snapshots every 5 min over a 240 min period. A noticeable "from darkness to brightness" phenomenon was observed for

both **TPEA** and DOX. The initial dark background indicated the stability of $\mathbf{1}_8$-**TPEA**-DOX in the cell culture medium, making them suitable for *in vitro* real-time visualization of intracellular stimulus-triggered drug release. Following this initial period of darkness, the areas containing lysosomes became bright, displaying orange and blue colors, signifying the awakening of both DOX and **TPEA** and the initiation of the fluorogenic process due to the disruption of $\mathbf{1}_8$-**TPEA**-DOX. Subsequently, the cell nucleus became light, indicating that DOX had reached its site of action.[41] Based on these results (Figure S20), we propose the following drug release process: $\mathbf{1}_8$-**TPEA**-DOX was taken up by the cells and transported to lysosomes. Within the lysosomes, owing to the acidic pH and higher GSH concentration, the nanofiber bundles began to break down. This disruption interrupted the ETR between DOX and **TPEA**, causing the quenched fluorescence to "wake up" and light the lysosomes. Subsequently, the released DOX from $\mathbf{1}_8$-**TPEA**-DOX entered the nucleus and exerted its anti-tumor function.

In conclusion, we have demonstrated that the energy derived from AIE's preorganization is multifaceted. It manifests not only as luminescence but can also be converted into chemical energy through catalysis for a reaction, with enhanced production selectivity resulting from AIE's steric effects. Such a complex chemical system operated by covalent reactions and noncovalent interactions also dictated the adaptation of structure and optical property to produce a multicomponent nanosystem to visualize the drug release process in real time. These findings have highlighted the energy transfer between supramolecular aggregation and *in situ* chemical reactions to evolve into functional multicomponent nanosystems for advanced applications. Our research has presented complex yet interesting molecular behaviors and functions at the systems level, orchestrating a harmonious dance of physical and chemical processes. Such advancements hint at the promising trajectory of systems chemistry, echoing nature's intricate complexities and heralding breakthroughs in realms like sensing, anti-counterfeiting, and electronics.

METHODS

Details regarding the methods can be found in the supplemental methods.

RESOURCE AVAILABILITY

Lead contact

Further information and requests for resources and reagents should be directed to and will be fulfilled by the lead contact, Dr. Jianwei Li (jianwei.li@utu.fi).

Materials availability

All stable and unique materials generated in this study are available from the lead contact upon reasonable request.

Data and code availability

All of the data supporting this study have been included in the article and supplemental information. Other related data are available from the corresponding authors upon reasonable request.

ACKNOWLEDGMENTS

We are grateful for the financial support from the Sigrid Jusélius Foundation (Senior Researcher Fellowship to J.L.) and the Academy of Finland (decision no. 318524, project funding to J.L.). J.Y. and X. Wu acknowledge the support from the China Scholarship Council. A.C.P. thanks Biocenter Finland for infrastructure support. We thank the Turku Center for Chemical and Molecular Analytics for providing NMR and the Electron Microscopy Laboratory, Institute of Biomedicine, University of Turku, and Biocenter Finland for TEM imaging. We thank Prof. M. Vilanova (Universitat de Girona, Spain) for her generous donation of the NCI/ADR-RES cells.

AUTHOR CONTRIBUTIONS

J.Y. conceived the idea, carried out the synthesis, characterization, and cell experiments, and wrote the manuscript. X. Wang and X. Wu helped with cell experiments. A.C.P. carried out the PXRD characterization. Y.L. and X. Wang carried out part of the synthesis. J.L. supervised the research and wrote the paper.

DECLARATION OF INTERESTS

The authors declare no competing interests.

SUPPLEMENTAL INFORMATION

Supplemental information can be found online at https://doi.org/10.1016/j.xcrp.2024.102355.

Received: September 2, 2024
Revised: October 31, 2024
Accepted: November 28, 2024
Published: January 15, 2025

REFERENCES

1. Lehn, J.-M. (1999). Dynamic combinatorial chemistry and virtual combinatorial libraries. Chem. Eur J. *5*, 2455–2463. https://doi.org/10.1002/(SICI)1521-3765(19990903)5:9<2455::AID-CHEM2455>3.0.CO;2-H.
2. Carnall, J.M.A., Waudby, C.A., Belenguer, A.M., Stuart, M.C.A., Peyralans, J.J.-P., and Otto, S. (2010). Mechanosensitive self-replication driven by self-organization. Science *327*, 1502–1506. https://doi.org/10.1126/science.1182767.
3. Lehn, J.-M. (2012). Constitutional dynamic chemistry: bridge from supramolecular chemistry to adaptive chemistry. Top. Curr. Chem. *322*, 1–32. https://doi.org/10.1007/128_2011_256.
4. Miljanić, O.Š. (2017). Small-molecule systems chemistry. Chem *2*, 502–524. https://doi.org/10.1016/j.chempr.2017.03.002.
5. Stingley, K.J., Carpenter, B.A., Kean, K.M., and Waters, M.L. (2023). Mismatched covalent and noncovalent templating leads to large coiled coil-templated macrocycles. Chem. Sci. *14*, 4935–4944. https://doi.org/10.1039/D3SC00231D.
6. Li, J., Nowak, P., and Otto, S. (2013). Dynamic combinatorial libraries: from exploring molecular recognition to systems chemistry. J. Am. Chem. Soc. *135*, 9222–9239. https://doi.org/10.1021/ja402586c.
7. Mattia, E., and Otto, S. (2015). Supramolecular systems chemistry. Nat. Nanotechnol. *10*, 111–119. https://doi.org/10.1038/nnano.2014.337.
8. Cao, Y., Yang, J., Eichin, D., Zhao, F., Qi, D., Kahari, L., Jia, C., Peurla, M., Rosenholm, J.M., Zhao, Z., et al. (2021). Self-Synthesizing Nanorods from Dynamic Combinatorial Libraries against Drug Resistant Cancer. Angew. Chem. Int. Ed. *60*, 3062–3070. https://doi.org/10.1002/anie.202010937.
9. Wu, X., Xing, J., Lyu, Y., Yu, J., Yang, J., Qi, D., Wang, X., Lin, J., Shao, G., Wu, A., and Li, J. (2023). Kinetic control over co-self-assembly using an in situ dynamic covalent reaction resulting in a synergistic

chemo-photodynamic therapy. Cell Rep. Phys. Sci. *4*, 101598. https://doi.org/10.1016/j.xcrp.2023.101598.

10. Wu, X., Zhang, D., Pan, T., Li, J., Xie, Y., Zhang, C., Pan, C., Zhang, Z., Lin, J., Wu, A., and Shao, G. (2023). Stimuli-Responsive Codelivery System Self-Assembled from in Situ Dynamic Covalent Reaction of Macrocyclic Disulfides for Cancer Magnetic Resonance Imaging and Chemotherapy. ACS Appl. Mater. Interfaces *15*, 44773–44785. https://doi.org/10.1021/acsami.3c10245.
11. Kriebisch, C.M.E., Burger, L., Zozulia, O., Stasi, M., Floroni, A., Braun, D., Gerland, U., and Boekhoven, J. (2024). Template-based copying in chemically fuelled dynamic combinatorial libraries. Nat. Chem. *16*, 1240–1249. https://doi.org/10.1038/s41557-024-01570-5.
12. Moulin, E., Cormos, G., and Giuseppone, N. (2012). Dynamic combinatorial chemistry as a tool for the design of functional materials and devices. Chem. Soc. Rev. *41*, 1031–1049. https://doi.org/10.1039/C1CS15185A.
13. Dumartin, M., Septavaux, J., Donnier-Maréchal, M., Jeamet, E., Dumont, E., Perret, F., Vial, L., and Leclaire, J. (2020). The dark side of disulfide-based dynamic combinatorial chemistry. Chem. Sci. *11*, 8151–8156. https://doi.org/10.1039/D0SC02399J.
14. Cougnon, F.B.L., Stefankiewicz, A.R., and Ulrich, S. (2024). Dynamic covalent synthesis. Chem. Sci. *15*, 879–895. https://doi.org/10.1039/D3SC05343A.
15. Gustafson, J., Nalbandian, C., and Hecht, D. (2016). The preorganization of atropisomers to increase target selectivity. Synlett *27*, 977–983. https://doi.org/10.1055/s-0035-1561314.
16. Warshel, A. (1998). Electrostatic origin of the catalytic power of enzymes and the role of preorganized active sites. J. Biol. Chem. *273*, 27035–27038. https://doi.org/10.1074/jbc.273.42.27035.
17. Biedermann, F., and Schneider, H.-J. (2016). Experimental binding energies in supramolecular complexes. Chem. Rev. *116*, 5216–5300. https://doi.org/10.1021/acs.chemrev.5b00583.
18. Hennefarth, M.R., and Alexandrova, A.N. (2022). Advances in optimizing enzyme electrostatic preorganization. Curr. Opin. Struct. Biol. *72*, 1–8. https://doi.org/10.1016/j.sbi.2021.06.006.
19. Luo, J., Xie, Z., Lam, J.W., Cheng, L., Chen, H., Qiu, C., Kwok, H.S., Zhan, X., Liu, Y., Zhu, D., and Tang, B.Z. (2001). Aggregation-induced emission of 1-methyl-1, 2, 3, 4, 5-pentaphenylsilole. Chem. Commun. *18*, 1740–1741. https://doi.org/10.1039/B105159H.
20. Hong, Y., Lam, J.W.Y., and Tang, B.Z. (2011). Aggregation-induced emission. Chem. Soc. Rev. *40*, 5361–5388. https://doi.org/10.1039/C1CS15113D.
21. Mei, J., Leung, N.L.C., Kwok, R.T.K., Lam, J.W.Y., and Tang, B.Z. (2015). Aggregation-induced emission: together we shine, united we soar. Chem. Rev. *115*, 11718–11940. https://doi.org/10.1021/acs.chemrev.5b00263.
22. Würthner, F. (2020). Aggregation-induced emission (AIE): a historical perspective. Angew. Chem. Int. Ed. *59*, 14192–14196. https://doi.org/10.1002/anie.202007525.
23. Zhang, Z., Kang, M., Tan, H., Song, N., Li, M., Xiao, P., Yan, D., Zhang, L., Wang, D., and Tang, B.Z. (2022). The fast-growing field of photo-driven theranostics based on aggregation-induced emission. Chem. Soc. Rev. *51*, 1983–2030. https://doi.org/10.1039/D1CS01138C.
24. Brzechwa-Chodzyńska, A., Markiewicz, G., Cecot, P., Harrowfield, J., and Stefankiewicz, A.R. (2023). Self-assembly of a fluorescent hydrogen-bonded capsule based on an amino-acid functionalised tetraphenylethylene. Chem. Commun. *59*, 6247–6250. https://doi.org/10.1039/D3CC01263H.
25. Xu, L., Jiang, X., Liang, K., Gao, M., and Kong, B. (2022). Frontier luminous strategy of functional silica nanohybrids in sensing and bioimaging: From ACQ to AIE. Aggregate *3*, e121. https://doi.org/10.1002/agt2.121.
26. Zheng, X., Zhu, W., Zhang, C., Zhang, Y., Zhong, C., Li, H., Xie, G., Wang, X., and Yang, C. (2019). Self-assembly of a highly emissive pure organic imine-based stack for electroluminescence and cell imaging. J. Am. Chem. Soc. *141*, 4704–4710. https://doi.org/10.1021/jacs.8b13724.
27. Li, J., Wang, J., Li, H., Song, N., Wang, D., and Tang, B.Z. (2020). Supramolecular materials based on AIE luminogens (AIEgens): construction and applications. Chem. Soc. Rev. *49*, 1144–1172. https://doi.org/10.1039/C9CS00495E.
28. Feng, F., Peng, Y., Zhang, L., and Huang, W. (2021). Imine organic cages derived from tetraphenylethylene dialdehydes exhibiting aggregation-induced emission and explosives detection. Dyes Pigments *194*, 109657. https://doi.org/10.1016/j.dyepig.2021.109657.
29. Feng, H.-T., Yuan, Y.-X., Xiong, J.-B., Zheng, Y.-S., and Tang, B.Z. (2018). Macrocycles and cages based on tetraphenylethylene with aggregation-induced emission effect. Chem. Soc. Rev. *47*, 7452–7476. https://doi.org/10.1039/C8CS00444G.
30. Lou, X.Y., and Yang, Y.W. (2018). Manipulating aggregation-induced emission with supramolecular macrocycles. Adv. Opt. Mater. *6*, 1800668. https://doi.org/10.1002/adom.201800668.
31. Li, G., and Li, Y.M. (2022). Modulating the aggregation of amyloid proteins by macrocycles. Aggregate *3*, e161. https://doi.org/10.1002/agt2.161.
32. Chang, D., Xiao, X., An, D., Zhang, R., Song, X., Liu, Y., Zhao, Y., and Lu, X. (2023). Facile synthesis of azobenzene-embedded conjugated macrocycles for optically switchable single-crystal transistors and tunable supramolecular assemblies. Aggregate *4*, e380. https://doi.org/10.1002/agt2.380.
33. Chen, M.Z., Moily, N.S., Bridgford, J.L., Wood, R.J., Radwan, M., Smith, T.A., Song, Z., Tang, B.Z., Tilley, L., Xu, X., et al. (2017). A thiol probe for measuring unfolded protein load and proteostasis in cells. Nat. Commun. *8*, 474. https://doi.org/10.1038/s41467-017-00203-5.
34. Otto, S., Furlan, R.L.E., and Sanders, J.K.M. (2002). Recent developments in dynamic combinatorial chemistry. Curr. Opin. Chem. Biol. *6*, 321–327. https://doi.org/10.1016/S1367-5931(02)00331-9.
35. Wang, P., Yan, X., and Huang, F. (2014). Host–guest complexation induced emission: a pillar [6] arene-based complex with intense fluorescence in dilute solution. Chem. Commun. *50*, 5017–5019. https://doi.org/10.1039/C4CC01560F.
36. Borjihan, Q., Wu, H., Dong, A., Gao, H., and Yang, Y.W. (2021). AIEgens for bacterial imaging and ablation. Adv. Healthc. Mater. *10*, 2100877. https://doi.org/10.1002/adhm.202100877.
37. Jawad, B., Poudel, L., Podgornik, R., Steinmetz, N.F., and Ching, W.-Y. (2019). Molecular mechanism and binding free energy of doxorubicin intercalation in DNA. Phys. Chem. Chem. Phys. *21*, 3877–3893. https://doi.org/10.1039/C8CP06776G.
38. Schmidt, M.F., and Rademann, J. (2009). Dynamic template-assisted strategies in fragment-based drug discovery. Trends Biotechnol. *27*, 512–521. https://doi.org/10.1016/j.tibtech.2009.06.001.
39. Xue, X., Zhao, Y., Dai, L., Zhang, X., Hao, X., Zhang, C., Huo, S., Liu, J., Liu, C., Kumar, A., et al. (2014). Spatiotemporal drug release visualized through a drug delivery system with tunable aggregation-induced emission. Adv. Mater. *26*, 712–717. https://doi.org/10.1002/adma.201302365.
40. Li, F., Chen, W.L., You, B.G., Liu, Y., Yang, S.d., Yuan, Z.Q., Zhu, W.J., Li, J.Z., Qu, C.X., Zhou, Y.J., et al. (2016). Enhanced cellular internalization and on-demand intracellular release of doxorubicin by stepwise pH-/reduction-responsive nanoparticles. ACS Appl. Mater. Interfaces *8*, 32146–32158. https://doi.org/10.1021/acsami.6b09604.
41. Xue, X., Jin, S., Zhang, C., Yang, K., Huo, S., Chen, F., Zou, G., and Liang, X.-J. (2015). Probe-inspired nano-prodrug with dual-color fluorogenic property reveals spatiotemporal drug release in living cells. ACS Nano *9*, 2729–2739. https://doi.org/10.1021/nn5065452.
42. Yonenuma, R., and Mori, H. (2023). Synthesis and self-assembly of a diphenylalanine–tetraphenylethylene hybrid monomer and RAFT polymers with aggregation-induced emission. Polym. Chem. *14*, 1469–1477. https://doi.org/10.1039/D2PY01602H.
43. Zhao, M., Lai, W., Li, B., Bai, T., Liu, C., Lin, Y., An, S., Guo, L., Li, L., Wang, J., and Zhang, F. (2024). NIR-II Fluorescence Sensor Based on Steric Hindrance Regulated Molecular Packing for In Vivo Epilepsy Visualization.

Angew. Chem. In. Ed. *63*, e202403968. https://doi.org/10.1002/anie.202403968.

44. Huang, W.-T., Chang, M.-C., Chu, C.-Y., Chang, C.-C., Li, M.-C., and Liu, D.-M. (2019). Self-assembled amphiphilic chitosan: A time-dependent nanostructural evolution and associated drug encapsulation/elution mechanism. Carbohydr. Polym. *215*, 246–252. https://doi.org/10.1016/j.carbpol.2019.03.083.

45. Yuan, Y., and Liu, B. (2017). Visualization of drug delivery processes using AIEgens. Chem. Sci. *8*, 2537–2546. https://doi.org/10.1039/C6SC05421H.

46. Mura, S., Nicolas, J., and Couvreur, P. (2013). Stimuli-responsive nanocarriers for drug delivery. Nat. Mater. *12*, 991–1003. https://doi.org/10.1038/nmat3776.

47. Estrela, J.M., Ortega, A., and Obrador, E. (2006). Glutathione in cancer biology and therapy. Crit. Rev. Clin. Lab Sci. *43*, 143–181. https://doi.org/10.1080/10408360500523878.

48. Bansal, A., and Simon, M.C. (2018). Glutathione metabolism in cancer progression and treatment resistance. J. Cell Biol. *217*, 2291–2298. https://doi.org/10.1083/jcb.201804161.

49. Lee, R.J., Wang, S., Turk, M.J., and Low, P.S. (1998). The effects of pH and intraliposomal buffer strength on the rate of liposome content release and intracellular drug delivery. Biosci. Rep. *18*, 69–78. https://doi.org/10.1023/a:1020132226113.

50. Manocha, B., and Margaritis, A. (2010). Controlled Release of Doxorubicin from Doxorubicin/γ-Polyglutamic Acid Ionic Complex. J. Nanomater. *2010*, 780171. https://doi.org/10.1155/2010/780171.

51. AlSawaftah, N.M., Awad, N.S., Pitt, W.G., and Husseini, G.A. (2022). pH-responsive nanocarriers in cancer therapy. Polymers *14*, 936. https://doi.org/10.3390/polym14050936.